

Dynamical and optical properties of warm dense hydrogen

L. A. Collins, S. R. Bickham,* J. D. Kress, and S. Mazevet
Theoretical Division, Los Alamos National Laboratory, Los Alamos, New Mexico 87545

T. J. Lenosky
Lawrence Livermore National Laboratory, Livermore, California 94551

N. J. Troullier
University of Minnesota, Minneapolis, Minnesota 55455

W. Windl
Computational Materials, Motorola, Inc., Austin, Texas 78721
 (Received 12 October 2000; published 20 April 2001)

We report dynamical and optical properties of hydrogen (deuterium) around the region of the principal Hugoniot that starts from the cryogenically cooled molecular liquid. These properties were determined by finite-temperature density functional (FTDF) molecular dynamics (MD) simulations within the local density and generalized gradient approximations. The principal Hugoniot, calculated from the FTDF-MD equation of state, agrees with gas-gun and recent laser-shock experiments for pressures up to 50 GPa. However, the maximum compression of the FTDF-MD Hugoniot (4.6 at 52 GPa) significantly differs from that of the laser shock experiment (6 at about 150 GPa). On the other hand, the optical reflectivities show reasonable agreement with the laser measurements for pressures up to 70 GPa. The system smoothly dissociates along the Hugoniot with the electrical conductivity reaching a value of $4000 \Omega^{-1} \text{cm}^{-1}$ at maximum compression. We also obtain good agreement with previous tight-binding and *ab initio* molecular dynamics studies.

DOI: 10.1103/PhysRevB.63.184110

PACS number(s): 61.20.Ja, 62.50.+p, 72.20.-i

I. INTRODUCTION

While the nature of dense hydrogen has always driven the modeling of such diverse systems as planetary interiors, inertial confinement fusion capsules, and pulsed-power produced plasmas,¹⁻⁴ recent gas-gun and laser experiments have provided new clues to its more intricate features. Starting from cryogenically cooled molecular hydrogen, the multi-shock gas gun experiments^{5,6} have pushed into new regimes at hydrogen densities on the order of 1 g/cm^3 at pressures up to 100 GPa and relatively low temperatures ($< 5000 \text{ K}$). As the pressure rises, the electrical conductivity of the fluid likewise increases to a value suggestive of a semiconductor ($\sim 3000 \Omega^{-1} \text{cm}^{-1}$). The system becomes a soup composed of molecules, atoms, and a few ions. A series of multiple-shock experiments,⁷ employing explosively driven plates, yielded similar behavior. In addition, single-shock laser studies^{8,9} on deuterium indicated that the principal Hugoniot predicted by theory¹⁰ might have serious defects. These experiments indicated a softening of the Hugoniot, allowing compressions of a factor of 6—resembling more an ideal rigid-rotor molecular gas. Such experiments have in turn generated renewed efforts in developing and perfecting various theoretical methods and models.

The most sophisticated methods include the path-integral Monte Carlo (PIMC) (Refs. 11,12) and density functional theory (DFT) molecular dynamics (MD). The DFT-MD approaches, in turn, include both direct diagonalization^{13,14} and Car-Parrinello¹⁵⁻¹⁷ and have generally operated in the local-density approximation (LDA). Recent applications of the generalized gradient approximation (GGA) (Refs. 18-20)

have relaxed the local-density constraints and provided simulations of enhanced accuracy. The computational intensity of these methods confines sample sizes and simulation times to fairly small values. In order to increase both, more approximate methods such as Thomas-Fermi,²¹ wave-packet molecular dynamics,²² and tight-binding (TBMD) (Refs. 23-25) have evolved. In addition to these dynamical schemes, models primarily based upon the minimization of the free-energy have also addressed this regime.^{10,26-28}

In earlier studies,^{13,24} we focused on the optical properties, in particular, the electrical conductivity, in the regime of the multiple-shock gas gun experiments.⁶ We found that the conductivity rose with increasing pressure, closely following the dissociation of the hydrogen molecules, and that the monomers contributed substantially to the mobility of the electrons through the fluid. The system consisted of a mixture of atoms and molecules in a highly transient state. For this paper, we concentrate on the region in and around the single-shock (principal) Hugoniot as examined in the laser experiments for which reflectivity measurements exist.

II. FORMULATION

We consider as a model of a dense medium a collection of N_a nuclei and N electrons in a cubic reference cell of length L . This choice defines a number density $\rho_n [= N_a/L^3]$ and an associated ion sphere radius $r_s [= (3/4\pi\rho_n)^{1/3}]$. To obtain a more tractable problem, we use the Born-Oppenheimer approximation by which the nuclear and electronic motion decouple. This condition naturally divides the evolution of the system into two stages. For a fixed nuclear configuration, a

fully quantum-mechanical treatment applies to the electrons. From an elaborate electronic structure calculation, we determine the force on each nucleus. This force in turn is used in the classical equations of motion to advance the nuclei. The procedure is repeated for each time step. We shall in the following sections briefly describe the basic parts of this quantum molecular dynamics (QMD) scheme since the details abound in other references.¹³

However, before proceeding, we should mention that this QMD approach exhibits great flexibility and predictive power and has seen many applications beyond those to hydrogen previously cited.^{13,18,24} These have included such eclectic processes as the rare-gas solids under extreme pressures,²⁹ liquid-vapor phase transitions in alkali metals,³⁰ shock compression of hydrocarbons³² and nitrogen,³¹ and defects and disorder in semiconductors.³³

A. Molecular dynamics

All of our simulations employ constant density and volume. Since we use a finite sample in a basic reference cell, we also invoke periodic boundary conditions by which a particle exiting the cell through one side is replaced by one entering on the opposite side. This convention preserves constant density within the cell. We consider both microcanonical and isokinetic ensembles. In the former, the system remains free to adjust to an average equilibrium ionic temperature T_i , and the total energy should be conserved. The degree to which energy conservation obtains provides an excellent diagnostic of the MD parameters, especially for the size of the time step. For the isokinetic ensemble, we fix the temperature at a prescribed value T_i and maintain this balance through a simple velocity scaling procedure.³⁴ In addition, we start the sample in a high symmetry state, such as body-centered cubic (bcc), and associate with each nucleus a random velocity consistent with a Maxwell-Boltzmann distribution at T_i . Successive application of a propagator, such as the Verlet algorithm,³⁴ evolves the system in time. The resulting collection of positions, velocities, and forces of the nuclei at each time step defines a trajectory.

In order to determine the quantum mechanical forces that operate on the nuclei, we rely upon density functional approaches. A finite-temperature density functional (FTDF) procedure,^{35,36} based upon the Mermin functional, provides a highly accurate determination of the forces. Minimizing this functional with respect to variations of the electron density leads to a set of equations for the electronic orbitals ψ_i and eigenvalues ϵ_i of the Kohn-Sham (KS) form

$$\left[-\frac{1}{2}\nabla^2 + V_{\text{ext}}(\mathbf{r}) + V_H(\mathbf{r}) + V_{\text{xc}}(\mathbf{r}) \right] \psi_i(\mathbf{r}) = \epsilon_i \psi_i(\mathbf{r}). \quad (1)$$

The first term represents the kinetic energy; the second term, the interaction with an external potential, usually taken as the electron-ion interaction; and the third, the Hartree term or Coloumbic interaction of a classical charge distribution. The final component gives the exchange-correlation interaction. Since terms in the KS equations depend on the density and the orbitals, these equations must be solved iteratively. The

orbitals are populated according to a Fermi-Dirac distribution $f_{\text{FD}}(\epsilon)$ at the electron temperature T_e with the electronic density given by

$$n(\mathbf{r}) = \sum_i f_{\text{FD}}(\epsilon_i) |\psi_i(\mathbf{r})|^2. \quad (2)$$

The sum runs over all states n_0 occupied down to a particular tolerance, usually $f_{\text{FD}} \sim 10^{-6}$. We expand the orbitals in a plane-wave (PW) basis and operate both within the local density and the generalized gradient³⁷ approximations for V_{xc} . In particular, the GGA methods provide a highly accurate means of studying the thermochemistry of chemical bonding by representing the inhomogeneities inherent in the electron charge density.

We replace the V_{ext} term with a pseudopotential; both the Troullier-Martins (TM) (Ref. 38) and the ultrasoft (US) (Refs. 39,40) forms have proved viable. In determining the forces on the nuclei, we generally assume local thermodynamic equilibrium (LTE) with the electron and ion temperatures equated [$T_e = T_i$] and include the nuclear-nuclear interaction contribution. The FTDF method, as discussed above, encompasses all manner of transient effects such as dissociation and association of chemical bonds, quasimolecular formation, and ionization and recombination.

The application of the MD algorithm produces at each time step a set of positions, velocities, forces, and electronic orbitals. This information provides the basis for the generation of basic system properties. For example, the total pressure consists of contributions from the electronic (P_e) and ionic (P_i) components. The former comes directly from derivatives taken with respect to the KS electronic orbitals⁴¹ while the latter arises from the ideal gas expression since the ions move classically. We thus have

$$P = P_e + \rho_n k_B T_i, \quad (3)$$

where k_B is the Boltzmann constant. The atom-atom pair correlation function $g(r)$ provides another useful diagnostic tool. This function gives the probability of finding an atom at a distance r from a reference atom. Finally, Green-Kubo formulas, based on autocorrelation functions, relate the trajectory information to microscopic properties of the system such as diffusion.³⁴ The properties we present represent averages over time once the system has reached an equilibrium.

In the regime under investigation, the fluid can have a complex nature with atoms, molecules, and ions all mixed together. The dissociation fraction β , the ratio of the number of monomers to the total number of particles, gives one measure of this complexity. We have used two complementary procedures¹³ to determine this quantity. The first employs a simple picture of the liquid by assuming that every atom not identified as belonging to a dimer is dissociated (a monomer). No larger molecular species are identified. If two atoms are each the nearest atom to one another, we call them a dimer. By counting the number of dimers n_2 , we arrive at a definition of the dissociation fraction

$$\beta = (N_a - 2n_2)/N_a. \quad (4)$$

We have also compared against an algorithm⁴² that counts all connected molecules (chains or clusters) within a certain prescribed bond length (r_{bond}) and found distributions consistent with our simple formulation. The program defines a species fraction x_γ

$$x_\gamma = \gamma n_\gamma / N_a, \quad (5)$$

where n_γ gives the number of clusters with γ associated atoms. From the definition, $\beta = n_1$. We usually select r_{bond} as the distance at which the spatial integral over $g(r)$ reaches unity.

We shall in the following descriptions generally employ atomic units with the energy, length, and time units given in hartrees (1 $\hbar = 27.2$ eV), bohr (1 $a_B = 5.29 \times 10^{-9}$ cm), and $\tau_{\text{a.u.}}$ (1 $\tau_{\text{a.u.}} = 2.42 \times 10^{-17}$ s), respectively.

B. Electrical conductivities and optical properties

The frequency-dependent conductivity $\sigma(\omega)$ has both real and imaginary parts:

$$\sigma(\omega) = \sigma_1(\omega) + i\sigma_2(\omega). \quad (6)$$

The real part (the usual electrical conductivity) is derived from the Kubo-Greenwood (KG) formulation^{43,44} as

$$\sigma_1(\omega) = \frac{2\pi}{\Omega} \sum_{ij} F_{ij} |D_{ij}|^2 \delta(\epsilon_i - \epsilon_j - \omega) \quad (7)$$

with Ω the atomic volume and ω the frequency. The other quantities include (1) the difference between the Fermi-Dirac distributions at a temperature T

$$F_{ij} = [f_{\text{FD}}(\epsilon_i) - f_{\text{FD}}(\epsilon_j)] / \omega \quad (8)$$

and (2) the velocity dipole matrix element

$$|D_{ij}|^2 = \frac{1}{3} \sum_\alpha |\langle \psi_i | \nabla_\alpha | \psi_j \rangle|^2. \quad (9)$$

The quantities ϵ_i and ψ_i represent the energy and wavefunctions of, for example, the i th orbital found from the diagonalization of the Kohn-Sham equations. The summation in i runs over all effectively occupied states while that in j covers only the remaining unoccupied ones for a total of n_s states. An analogous integral expression follows from the properties of the product delta function as

$$\sigma_1(\omega) = \frac{2\pi}{\Omega^3} \int F[E', E] |D(E' | E)|^2 N(E') N(E) dE, \quad (10)$$

where the density of states per unit energy per unit volume has the form

$$N(E) = \frac{1}{\Omega} \sum_i \delta(E - \epsilon_i), \quad (11)$$

$E' = E + \omega$ and $D(E' | E)$ is the analog of Eq. (9) for a continuous range of energies. The integral spans all occupied orbitals up to the Fermi energy ϵ_F . A useful check arises from a simple sum rule⁴⁵

$$S \equiv \frac{2}{\pi n_e} \int \sigma_1(\omega) d\omega = 1, \quad (12)$$

where n_e is the electron number density (electrons/ a_B^3). The departure of S from unity gives a measure of the accuracy of the calculated conductivity. Finally, we define the dc conductivity as $\sigma_{\text{dc}} = \sigma_1(0)$.

Other properties follow directly from a knowledge of the frequency-dependent real-part of the conductivity.⁴⁵ While fairly standard, we repeat these definitions as slightly different conventions remain in vogue. The imaginary part arises from the application of a Kramers-Kronig relation as

$$\sigma_2(\omega) = -\frac{2}{\pi} P \int \frac{\sigma_1(\nu) \omega}{(\nu^2 - \omega^2)} d\nu, \quad (13)$$

where P stands for the principal value of the integral. The dielectric functions then follow immediately from the two parts of the conductivity:

$$\epsilon_1(\omega) = 1 - \frac{4\pi}{\omega} \sigma_2(\omega), \quad (14)$$

$$\epsilon_2(\omega) = \frac{4\pi}{\omega} \sigma_1(\omega). \quad (15)$$

The real (n) and imaginary (k) parts of the index of refraction are in turn related to the dielectric function by a simple formula:

$$\epsilon(\omega) = \epsilon_1(\omega) + i\epsilon_2(\omega) = [n(\omega) + ik(\omega)]^2 \quad (16)$$

or

$$n(\omega) = \frac{1}{2} \sqrt{|\epsilon(\omega)| + \epsilon_1(\omega)} \quad (17)$$

$$k(\omega) = \frac{1}{2} \sqrt{|\epsilon(\omega)| - \epsilon_1(\omega)}. \quad (18)$$

Finally, these quantities define a reflectivity (r) and an absorption coefficient (α):

$$r(\omega) = \frac{[1 - n(\omega)]^2 + k(\omega)^2}{[1 + n(\omega)]^2 + k(\omega)^2} \quad (19)$$

$$\alpha(\omega) = \frac{4\pi}{n(\omega)} \sigma_1(\omega). \quad (20)$$

While we have used atomic units to represent the general formulas, we also express conductivities in units of inverse Ω cm (1 Ω^{-1} cm⁻¹ = 9×10^{11} s⁻¹ = 2.18×10^{-5} atomic units). In addition, we shall sometimes report the optical properties in terms of energies ($\hbar\omega$) or wavelengths ($\lambda = 2\pi c/\omega$).

We evaluate the integral in Eq. (10) by partitioning into energy bins of equal size ΔE and determining average quantities within each bin from the discrete eigenstate calculations. Since the delta function causes $\sigma(\omega)$ to peak around ω , we can use Eq. (7) directly and similarly define an aver-

age conductivity.¹⁷ The production of only a finite number of eigenstates places a restriction on the frequency range. We can obtain converged values of $\sigma(\omega)$ only for $\omega \leq |\epsilon_{n_s} - \epsilon_f|$ since larger values of ω connect to unoccupied excited states ϵ_i with $i \geq n_s$.

Since the electronic structure programs produce a finite number of eigenenergies and finite frequency differences, we cannot determine the dc conductivity directly. Instead, we must extrapolate to the zero frequency limit. No unique prescription exists for this procedure. We have tried several methods including least-squares polynomial fits and the simple Drude form^{44,17}

$$\sigma_1(\omega) = \frac{\sigma_{\text{dc}}}{1 + \omega^2 \tau_D^2}, \quad (21)$$

where τ_D represents an effective collision time. In this case, we determine τ_D and σ_{dc} from a two-parameter least-squares fit. The Drude form only applies when $d\sigma_1/d\omega < 0$ as ω goes to zero.

The above formulas apply for a spatial configuration of the atoms at a single time step within an MD trajectory. We report a trajectory-averaged optical property given by

$$\chi = \frac{1}{n_{\text{snap}}} \sum_{r=1}^{n_{\text{snap}}} \chi_r, \quad (22)$$

where χ_r depicts a representative optical property calculated for a selected configuration r from the MD simulation and n_{snap} is the number of representative configurations or snapshots employed. The configurations are spaced at time steps separated by at least the correlation time, the e -folding time of the velocity autocorrelation function.

III. RESULTS AND DISCUSSION

A. MD simulations

Since the interaction potentials do not depend upon mass, we need only perform MD simulations for one isotopic species, in this case hydrogen, to obtain static, dynamical, and optical properties. Simple scaling rules then suffice to determine these properties for deuterium and tritium. For example, pressure (P), temperature (T), electrical conductivity (σ_1), and species fraction (x_i) all change according to the number density ρ_n or r_s . Therefore, samples of hydrogen and deuterium with mass densities of $\rho(\text{H})$ and $\rho(\text{D}) = 2\rho(\text{H})$, respectively, will have the same pressure P since they correspond to the same ρ_n . On the other hand, the diffusion coefficient scales as

$$D_j = \sqrt{\frac{1}{A_j}} D_{\text{H}}, \quad (23)$$

where A_j is the atomic weight of deuterium or tritium and D_{H} corresponds to hydrogen. We shall use these rules to examine both hydrogen and deuterium in the following discussion.

We employed the VASP plane-wave pseudopotential code, developed at the Technical University of Vienna,⁴⁶ at the

TABLE I. Comparison of properties: LDA, GGA, and TB methods at $T=5000$ K and $r_s=2$. PP refers to the pseudopotential, either ultrasoft (US) or Troullier-Martins (TM). $P_i=13.9$ GPa for all cases. $N_a=128$. Quantities in brackets represent powers of 10.

Method	PP	P_e (GPa)	P (GPa)	D_H (cm ² /s)
LDA	US	5.0	18.9	5.0[-3]
LDA	TM	7.6	21.5	5.0[-3]
GGA	US	10.1	24.4	4.2[-3]
TB		12.8	26.7	4.3[-3]

GGA level in an isokinetic ensemble to produce most of the MD trajectories in our analysis. A sample size of 128 hydrogen atoms with integrals performed at the Γ point and with a PW cutoff at 400 eV for 150 orbitals proved sufficient to produce accurate dynamical and electrical properties. In addition, we performed calculations with the PW molecular dynamics program PW6 (Ref. 47) in the LDA with the Troullier-Martins (TM) pseudopotential for cutoffs of $1.0a_B$ and 500 eV. Typical trajectories ran for 1 ps at time steps of 0.5 fs for temperatures below 15 000 K; higher temperatures required a shorter time step of 0.25 fs. The systems equilibrate very rapidly, usually within 200 time steps (~ 100 fs) after which temporal averages could safely be extracted. As a check, we have performed longer simulations out to 3 ps but observe changes of less than a few percent in the basic properties.

As an indication of the sensitivities, we make a representative comparison of the pressure and diffusion coefficients for several models at $T=5000$ K and $r_s=2$ in Table I. VASP runs include both LDA and GGA Hamiltonians with an ultrasoft (US) pseudopotential. For completeness, tight-binding results²⁴ are included. The electronic pressure represents the most sensitive quantity as it depends upon taking derivatives with respect to the wave function and involves no additional particle averages as do many of the autocorrelation functions. However, the total pressure, necessary for Hugoniot and experimental comparison, shows much less sensitivity due to the large ionic component. The difference among the different DFT approximations declines with increasing temperature and density.

In Table II, we present a variety of properties from the GGA calculations as a function of temperature and density. The diffusion coefficient D at a constant density shows a rapid rise with increasing temperature. This follows roughly similar increases in β and σ_{dc} . On the other hand, for a fixed temperature, D displays much less sensitivity to density changes. This result presents no surprises as the rapid temperature increase reflects the rise in the thermal energy as well as a secondary contribution from dissociation. On the other hand, a density change by only a factor of two does not substantially alter the basic interactions, which depend upon the interparticle separation that goes as the cube root of the density.

B. Hugoniot

Since we shall target results on or near the principal Hugoniot, we give a brief review of the current status of

TABLE II. Pressure (P), diffusion coefficient (D_H), dc conductivity (σ_{dc}), and dissociation fraction (β) from GGA-MD simulations with US pseudopotential at various densities and temperatures. Mass density $\rho(H)$ is for hydrogen. Last three entries, referred to in the text as PH1, PH2, and PH3, represent points on the Hugoniot. Quantities in brackets represent powers of 10.

r_s	$\rho(H)$ (g/cm ³)	P (GPa)	T (K)	D_H (cm ² /s)	σ_{dc} (Ω cm) ⁻¹	β
1.72	0.525	60.6	5000	5.0[-3]	4000	0.28
		87.8	10000	1.2[-2]	6000	0.33
1.85	0.422	37.9	5000	5.1[-2]	1600	0.22
		46.6	7500	9.9[-3]	3200	0.30
		57.4	10000	1.4[-2]	4000	0.34
		103.4	20000	3.6[-2]	4600	0.37
1.95	0.361	152.8	30000	5.0[-2]	4700	0.40
		27.0	5000	4.4[-3]	1300	0.17
		34.2	7500	1.0[-2]	2300	0.28
		41.9	10000	1.5[-2]	2800	0.31
		79.8	20000	3.8[-2]	3600	0.38
2.00	0.334	122.6	30000	6.0[-2]	3800	0.39
		18.7	2000	8.1[-4]	0	0.03
		24.4	5000	4.0[-3]	1000	0.16
		36.1	10000	1.7[-2]	2600	0.27
		54.1	15000	2.8[-2]	3300	0.34
1.96	0.355	72.5	20000	4.1[-2]	3700	0.38
		26.4	4600	3.6[-3]	1000	0.14
		1.90	0.391	49.0	9870	1.6[-2]
1.92	0.381	98.1	22300	4.0[-2]	4100	0.34

models and experiments related to this important quantity. In Fig. 1, we present a selective collection of the most recent results for the deuterium Hugoniot. The system starts as a cryogenically cooled liquid at $\rho_o(D)=0.171$ g/cm³. The points in pressure-density space then follow from the application of the single-shock Rankin-Hugoniot conditions based on the equation of state for a given theoretical model. At present, a large difference exists among various methods and the NOVA experiments.⁸ The SESAME,¹⁰ TB,²⁴ DFT-MD,¹⁸⁻²⁰ and PIMC (Ref. 12) equations of state (EOS), all appear in good agreement, giving a maximum compression $\eta=\rho/\rho_0$ of around 4. This value closely matches that for an ideal atomic fluid. The TB and GGA have maximum compressions of 4.3 and 4.6, respectively, with the PIMC lying in between. Therefore, at this juncture, the *ab initio* approaches closely concur as further confirmed in Fig. 2, which compares pressure as a function of temperature at a fixed density [$r_s=2$; $\rho(D)=0.668$ g/cm³]. However, they differ substantially from the lone experimental result,⁸ which yields $\eta=6$, a value more similar to an ideal rigid-rotor molecular fluid.

Many explanations have arisen to reconcile these findings, but no satisfactory resolution has occurred. At first, dissociation of molecular hydrogen appeared as a possible candidate. However, all the models displayed in Fig. 1 have some representation of this process including SESAME. In fact, the GGA formulation gives very good descriptions of the mol-

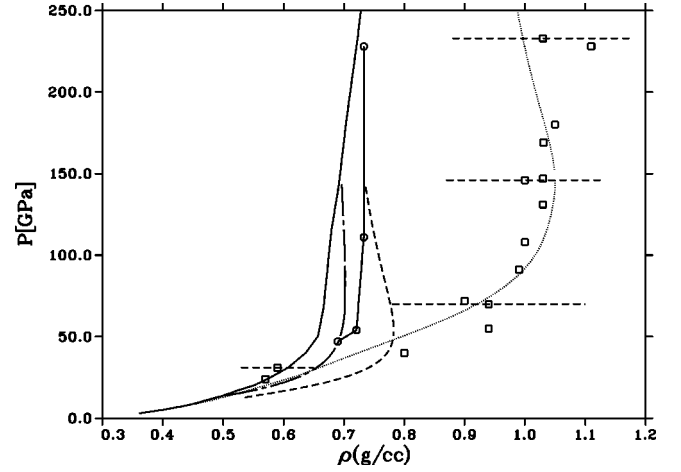


FIG. 1. Deuterium Hugoniot. Theoretical models: GGA-MD (long dash line); SESAME (solid line, Ref. 10); TB (chain, Refs. 24,25); Ross (dot, Ref. 27); and PIMC (solid-circles, Ref. 12). Experiments: laser (squares, Refs. 8).

ecules H₂ and H₄ out to fairly large separations of the atomic species [$\leq 4a_B$] as well as the basic solid structures. Other explanations centered on various phase transitions; however, an examination of Table II for $r_s=2$ demonstrates that the dissociation process proceeds smoothly as judged from the behavior of β as a function of temperature and pressure. While this represents a constant density demonstration, the Hugoniot in the realm of the maximum compression maintains a fairly constant ρ as indicated in Table III. Both the TB (Ref. 24) and PIMC (Ref. 12) show similar trends with no marked discontinuities.

Another posited explanation relies upon ionization mechanisms. Again, all the *ab initio* models have representations of excitation and ionization. In fact, the large energy cutoff in the DF approaches produce PW bases with tens of thousands of functions, which have a particular facility in depicting diffuse orbitals. The equally large number of states included in the formation of the KS density also guarantees a

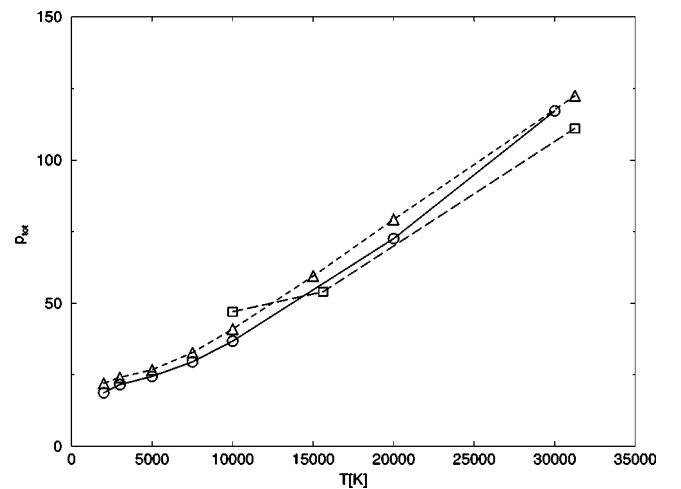


FIG. 2. Comparison of methods: Pressure as a function of temperature for $r_s=2$. Nomenclature: GGA (solid circles); TB (short-dash triangles); PIMC (long-dash squares).

TABLE III. Principal Deuterium Hugoniot points from GGA EOS for $\rho_0(\text{D})=0.171 \text{ g/cm}^3$ and $P_0=0$.

$\rho(\text{D}) \text{ (g/cm}^3\text{)}$	$T \text{ (K)}$	$P \text{ (GPa)}$	$u_s \text{ (km/s)}$
0.663	3740	21.3	13.0
0.708	4590	25.9	14.2
0.753	6210	33.5	16.0
0.780	9150	45.5	18.5
0.783	10840	52.0	19.8
0.780	14600	66.3	22.3
0.771	18640	81.2	24.8
0.759	23650	99.9	27.5

full representation of excitation processes. The FTDF provides an average surface based on the FD statistics along which the system evolves. We generally run in LTE with T_e set to T_i . However, we have also performed FTDF MD simulations with T_e ranging over values from 0 to 100 000 K, which changes the propagation surface. The basic parameters show very little sensitivity to this choice. In addition, tests⁴⁸ with models that include explicit interchanges of electronic surfaces indicate that the FTDF formulations probably work well in the regime considered.

C. Optical properties

1. Determination of σ_1

Our discussion of the optical properties begins with the details of several representative calculations. Since the principal optical properties derive from the real-part of the electrical conductivity σ_1 , we initially concentrate on this quantity. In general, σ_1 was determined from snapshots from either GGA or LDA molecular dynamics trajectories, using PW6 in the LDA with a TM pseudopotential having an r_c of $1.4a_B$. This cutoff gave results in close agreement with the US pseudopotential employed in VASP.

For several representative cases, we have checked at the LDA level against the independent programs of Pfaffen-zeller and Hohl(PH) (Ref. 17) and of CASTEP, a commercial code implemented in the CERIU2 package by Molecular Simulations, Inc., and found excellent agreement. For example, at $r_s=1.5$ and $T=2000 \text{ K}$, $\sigma_1(E)$ agreed to within 10% at the discrete energy points with the result of PH, who also employed a TM pseudopotential but truncated at $r_c=0.3$ rather than 1.4 bohr. The same extrapolation procedure yielded similar dc conductivities; in our case $2100 \Omega^{-1} \text{ cm}^{-1}$ as compared to 2200 for PH. Comparable comparisons against CASTEP runs, which used no pseudopotential approximation (bare nucleus), at $r_s=2$ at 5000 K also gave results within 10% of the TM ($r_c=1.4$) case as a function of energy E . These studies indicate that $\sigma_1(E)$ remains fairly insensitive to the pseudopotential form in this regime. In addition, both the delta function [Eq. (7)] and integral [Eq. (10)] formulations produce results within a few percent. We should also note that the LDA and GGA generally underestimate the band gap between occupied and unoccupied states and therefore may give conductivities somewhat high.

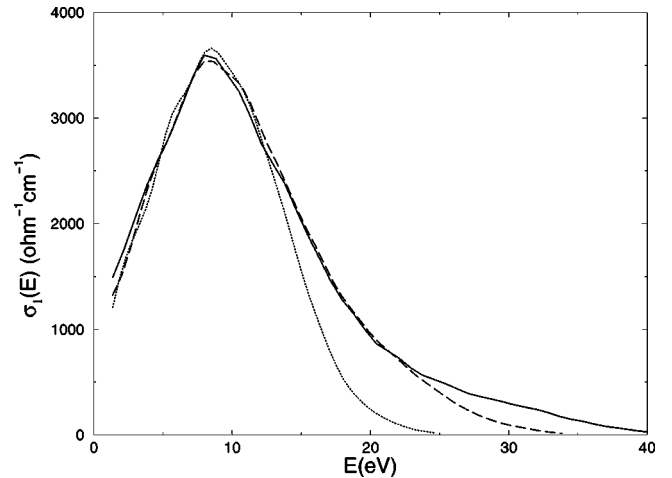


FIG. 3. Sensitivity of real electrical conductivity to the number of states. $n_s=150$ (dot), 250 (dash), and 350 (solid) for $r_s=2$ and $T=5000 \text{ K}$.

For the range of densities and temperatures considered, choosing the number of occupied states n_0 at 150 proved sufficient to converge the KS equations and therefore the forces for the MD propagation. However, the determination of σ_1 also includes a sum over unoccupied states. To properly converge the optical properties may take considerably more states than to converge the forces ($n_s > n_0$). Since the computational time for an MD step depends critically on the number of roots n_s extracted, we generally calculate optical properties only at a few selected snapshots (n_{snap}) along the MD simulation. Usually the average over five to ten snapshots, extracted from the later stages of the trajectory, suffices to produce well converged optical properties. We present in Fig. 3 the real part of the electrical conductivity as a function of the total number of states n_s at a representative density and temperature of $r_s=2$ and $T=5000 \text{ K}$. The quantity S [Eq. (12)] has values of 0.71, 0.87, and 0.92 for n_s of 150, 250, and 350, respectively, giving a quality measurement across the whole energy spectrum. However, the low frequency part converges much faster in regards to n_s . Therefore, the dc conductivity and reflectivity at low energies have stabilized long before S reaches unity. Figure 4 examines the convergence trends in states for the reflectivity. Given these findings, we have employed an n_s of at least 250 for all subsequently reported optical quantities since for this study our interest centers on low energies ($<10 \text{ eV}$).

Due to the finite basis set employed, we only obtain solutions to the KS equations at a discrete number of energies ϵ_i . This requires interpolation to produce intermediate energies and extrapolation to determine the dc electrical conductivity $\sigma_1(0)$. For temperatures below 10 000 K, a simple low-order polynomial fit to the lowest few values of $\sigma_1(\omega)$ is adequate. Still, due to the rapid decline in the conductivity approaching zero frequency, errors of up to 50% may arise for values below about $1000 \Omega^{-1} \text{ cm}^{-1}$. At temperatures above about 10 000 K, the conductivity generally increases with decreasing frequency and a least-squares fit to a Drude form gives a reasonable representation as indicated in Fig. 5 for $r_s=1.85$ and 30 000 K. The errors in this regime range

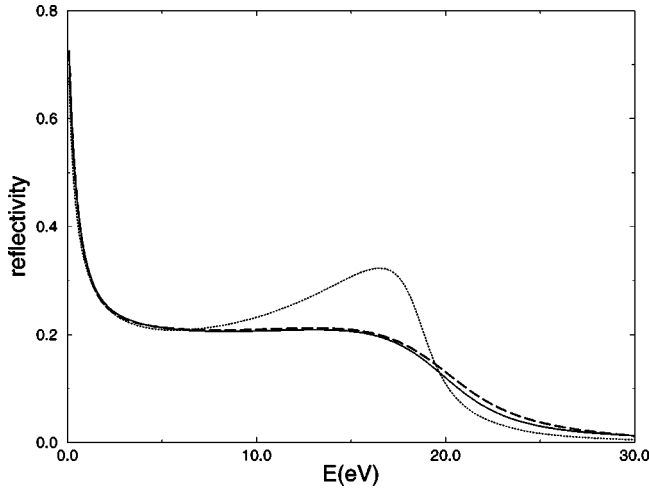


FIG. 4. Sensitivity of reflectivity to the number of states. $n_s = 150$ (dot), 250 (dash), and 350 (solid) for $r_s=2$ and $T = 5000$ K.

more on the order of 25%. We present σ_{dc} in Table II as a function of temperature and density.

Using the real part of the electrical conductivity determined from the GGA and KG calculations, we calculate the imaginary part σ_2 from the principal-value integral in Eq. (13)). An example appears in Fig. 6 for our standard case at $r_s=2$ and 5000 K. From these two quantities, all the other optical properties such as absorption, reflectivity, and dielectric functions derive.

2. Comparisons

We find good agreement between the GGA and our earlier TB studies²⁴ for pressure, diffusion, and dc electrical conductivity as indicated in Table IV. The TB employs but a single s -type orbital on each atomic site and the simple Mott formula for σ_{dc} . Some departure occurs at the higher temperatures probably due to the thinning number of TB states

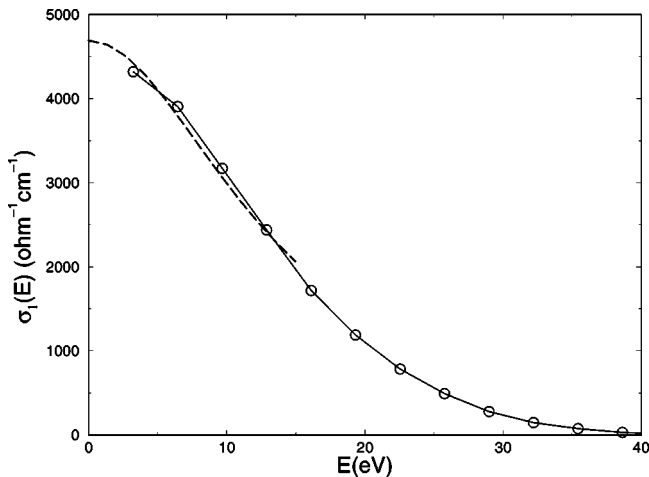


FIG. 5. Electrical conductivity as a function of energy at $r_s = 1.85$ and $T = 30000$ K. Nomenclature: solid line—DF and dashed line—Drude fit to first five DF points. Circles represent discrete results.

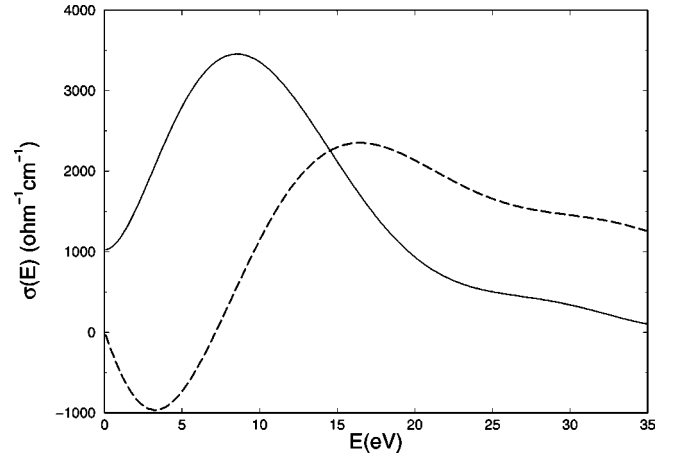


FIG. 6. Real (solid) and imaginary (dash) parts of the electrical conductivity at $r_s=2$ and 5000 K.

and applicability of the Mott form. We also find close agreement with the GGA calculations of Galli *et al.*¹⁹ with our electrical conductivity about 20% lower than their result at $\rho(H) = 1$ g/cm³ and 10000 K. Finally, Berkovsky⁴⁹ found similar trends for conductivity and reflectivity, using a thermodynamical Green's function approach combined with a hydrodynamical theory.

3. Trends in optical properties

Given recent experimental measurements, we focus particularly on the reflectivity. Figure 7 displays the dependence of $r(E)$ on temperature for a fixed density ($r_s=2$). This behavior remains typical for the range of densities explored from $\rho(D) = 0.6$ to 1.2 g/cm³, which spans the major features of the principal Hugoniot. These cases correspond to electrical conductivities of the order of a few thousand inverse Ω cm (see Table II). Thus, even a small σ_1 can produce substantial reflectivities. Large values of the reflectivity therefore need not indicate a highly conductive metallic state. We compare our values for $r(E)$ against those determined by the NOVA experiments at two wavelengths, 1064

TABLE IV. Comparison of GGA (upper entry) and TB (lower entry) models at $r_s=2$ as a function of temperature. Quantities in brackets represent powers of 10.

T (K)	P (GPa)	D_H (cm ² /s)	σ_{dc} (Ω cm) ⁻¹	β
2000	18.7	8.1[-4]	0	0.03
	22.0	8.8[-4]	4	0.05
5000	24.4	4.0[-3]	1000	0.16
	26.7	4.3[-3]	670	0.17
10000	36.1	1.7[-2]	2600	0.27
	40.9	1.6[-2]	2200	0.32
15000	54.1	2.8[-2]	3300	0.34
	59.4	3.3[-2]	2780	0.37
20000	72.5	4.1[-2]	3700	0.38
	79.2	4.3[-2]	2400	0.40

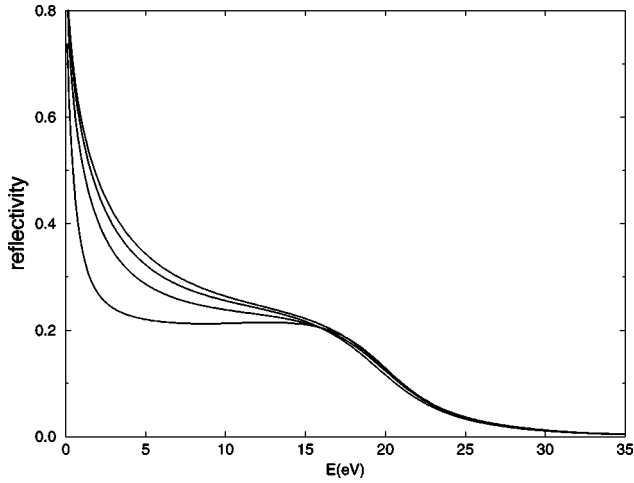


FIG. 7. Comparison of reflectivity at $r_s=2$ at temperatures of 5000, 10 000, 15 000, and 20 000 K. Lowest temperature corresponds to lowest curve.

nm (1.17 eV) and 808 nm (1.53 eV). The experimental results were reported as functions of the shock velocity. We have converted these to pressure values using the basic Rankin-Hugoniot relation

$$P = P_0 + (\rho_0 u_s^2 / \eta) (\eta - 1), \quad (24)$$

and the GGA equation of state (EOS). The regime in which the reflectivity rises sharply shows little sensitivity to the choice of EOS. As seen from Fig. 1, all the various models give basically the same behavior of the Hugoniot in this realm.

Figures 8 and 9, together with Table V, present three cases based on the GGA-MD calculations. The first, designated by the three filled squares, represents optical properties determined at points lying on the principal Hugoniot (see Table II). The second, given by the filled circles connected with a solid line, presents $r(E)$ along a constant density line ($r_s=2$) that closely follows the Hugoniot in the vicinity of

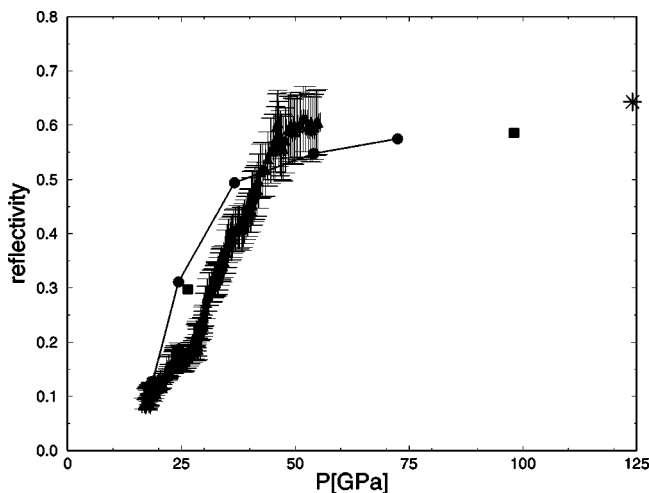


FIG. 8. Reflectivity at 1064 nm. Solid curves—GGA at $r_s=2$; solid squares—GGA Hugoniot points; stars—GGA off-Hugoniot point; and triangles with error bars—experiment (Ref. 9).

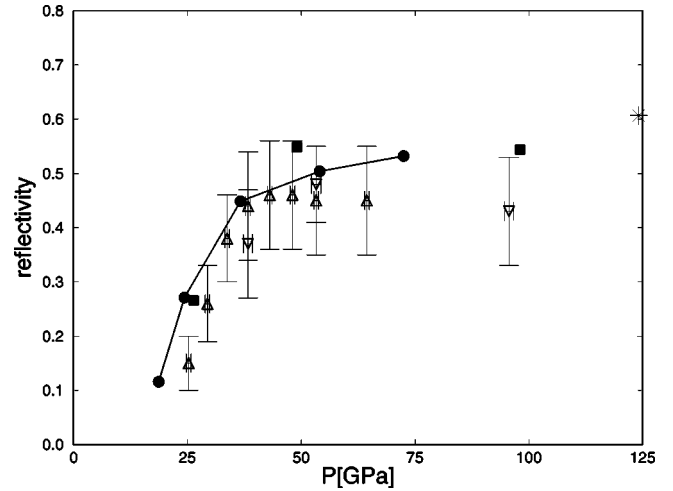


FIG. 9. Reflectivity at 808 nm; labels same as previous figure.

maximum compression. The third, marked by a star, gives the reflectivity at a density ($\rho=1 \text{ g/cm}^3$, $r_s=1.75$) and temperature ($T \sim 18,000 \text{ K}$) near the predicted maximum compression ($\eta \sim 6$) of the NOVA experiment. This point lies off the principal Hugoniot determined by the MD-GGA.

The figures show good agreement between the GGA and experimental results, especially in the general form and magnitude of the reflectivity. We note that the first case also exhibits a slight decline in $r(E)$ at high pressure as suggested by the experiments. In addition, the third case, which represents an off-Hugoniot point, indicates only a weak sensitivity to density and temperature, once saturation has been reached. This implies that reflectivity in this regime does not clearly discriminate among the various theoretical models. Finally, given the approximations involved, the GGA-MD results will generally show more sensitivity at the lower energies (longer wavelengths).

4. Nature of the fluid

We turn our attention to the actual nature of the fluid as it moves along the principal Hugoniot. The system initially consists entirely of molecules (D_2) at very low temperatures. As the compression occurs, the fluid heats and begins to dissociate. As indicated in Table II, the dissociation progresses in a steady, continuous manner, reaching about 30% ($\beta=0.3$) at the maximum compression point of the

TABLE V. Reflectivity $r(\lambda)$ as a function of wavelength and pressure for $r_s=2$ from GGA-MD simulations with US pseudopotential.

T (K)	P (GPa)	$r(\lambda)$		
		1064 nm	808 nm	404 nm
2000	18.7	0.128	0.116	0.097
5000	24.4	0.311	0.271	0.217
10 000	36.7	0.494	0.449	0.344
15 000	54.1	0.548	0.504	0.393
20 000	72.5	0.575	0.532	0.420

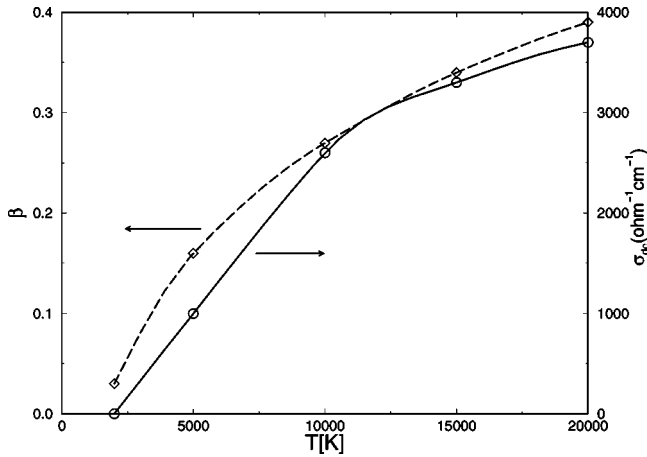


FIG. 10. Comparison of dc electrical conductivity σ_{dc} (solid) and dissociation fraction β (dash) for $r_s=2$ as a function of temperature.

GGA Hugoniot [$\rho(D) \sim 0.78 \text{ g/cm}^3$ and $T \sim 10\,000 \text{ K}$]. The medium continues to dissociate as it moves up the Hugoniot. Concomitantly, the electrical conductivity smoothly rises to values on the order of $3000\text{--}4000 \text{ } \Omega^{-1} \text{ cm}^{-1}$. The magnitude suggests a semiconductor or semimetal.

We examine this behavior more closely by considering a representative sample with a fixed density ($r_s=2$) and changing temperature. Figure 10 displays again the close relationship between conductivity and dissociation, indicating the important role played by the monomers. In this regime, the principal contribution to the dc conductivity comes from the states around the Fermi energy since the function F_{ij} [Eq. (8)] strongly peaks at ϵ_F . As illustrated in Fig. 11, for the lowest temperature (2000 K), very few states exist within a gap in $N(E)$ around ϵ_F , and the medium exhibits practically no metallic features. This gap, roughly fixed by the density, then fills with states as the temperature increases, yielding a rise in σ_{dc} . The conductivity saturates with rising tempera-

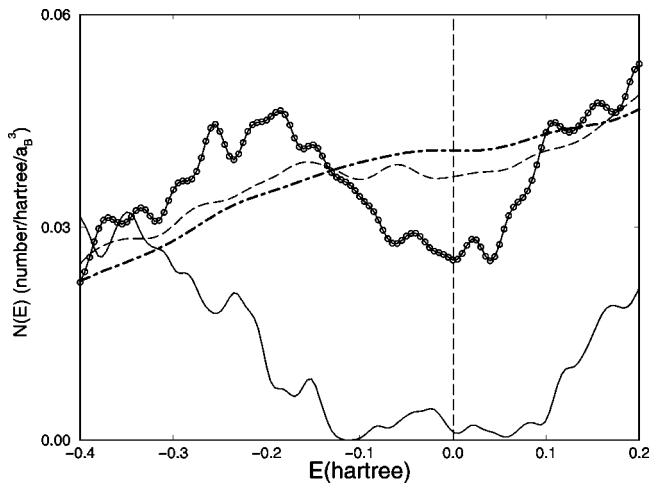


FIG. 11. Density of states $N(E)$ as a function of energy at $r_s=2$ for four temperatures: 2000 K (solid), 5000 K (circles), 10000 K (dash), and 20000 K (dash-dot). The dashed vertical line gives the Fermi energy.

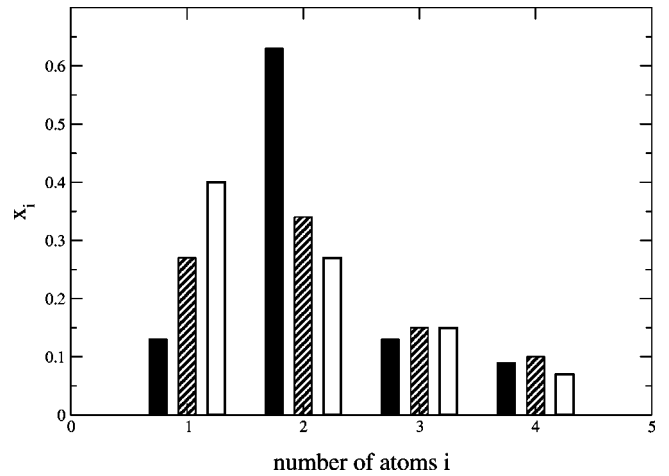


FIG. 12. Species fraction x_i along the principal deuterium Hugoniot. Nomenclature: filled—PH1 ($0.710 \text{ g/cm}^3, 4600 \text{ K}$); hatched—PH2 ($0.781 \text{ g/cm}^3, 9870 \text{ K}$); and clear—PH3 ($0.762 \text{ g/cm}^3, 22\,300 \text{ K}$). Points in $(\rho(D), T)$ -space correspond to last three entries in Table II. $x_1 = \beta$.

ture as the gap completely fills. The fluid resembles a weakly conducting medium with a mixture of atoms and molecules.

The structure of the fluid becomes clearer by considering the species fraction x_i and the pair correlation function along the Hugoniot. We consider the three last entries in Table II and for convenience, label them PH1, PH2, and PH3 respectively. They correspond to positions on the Hugoniot before (PH1), at (PH2), and after (PH3) maximum compression. Figure 12 shows, as noted before, that the fluid changes from primarily diatomic to atomic from PH1 to PH3. A study of the pair correlation function in Fig. 13 confirms this observation. The first peak corresponds to the average internuclear separation ($1.4 a_B$) for D_2 . As the temperature rises, this peak disappears indicating a transition to a more atomic character.

Since other studies^{15,17,13,50,51} have found complex clustering in hydrogen fluids in various temperature and density

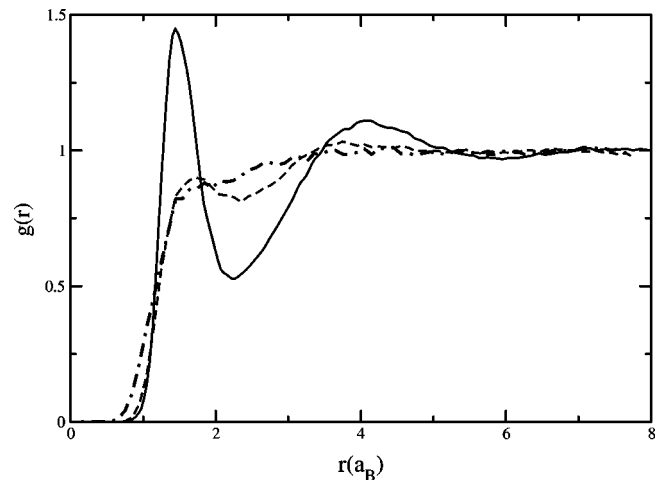


FIG. 13. Pair correlation functions $g(r)$ along the principal Hugoniot. Nomenclature: solid line—PH1, dashed line—PH2, and dash-dot line—PH3.

ranges, we have examined our trajectories for such behavior. The cluster analysis indicates a reasonable fraction ($\sim 20\%$) of atoms in D_3 and D_4 . However, this analysis presents only a trajectory average and must be tempered by the actual time these clusters remain together. Such analysis shows that only the dimer remains together for an interval long compared to the vibrational period of the ground state D_2 molecule (~ 5 fs). The larger clusters exist for only a fraction of this characteristic time, demonstrating that these structures do not form long-lived bonded complexes but more resemble ephemeral associations of atoms. Therefore, no polymer strings appear, and the particles engage in a state of rapid flux.

The description above of a transient fluid of interacting atoms and molecules with an electrical conductivity similar to a semiconductor, seems familiar. In fact, we have experienced just such a system in our earlier studies^{13,24} of the multiple-shock gas gun experiments.⁶ In this case, the correlated rise in dissociation and conductivity arose more from density rather than temperature effects. The final form of the systems, though, appear remarkably similar. This seems to indicate that the gas gun and laser experiments have probed the same basic medium in different temperature-density regimes.

IV. SUMMARY

We have determined dynamical and optical properties of hydrogen (deuterium) around the region of the principal Hugoniot that starts from the cryogenically cooled molecular

liquid. Temperature-dependent density functional molecular dynamics simulations within the local density and generalized gradient approximations provided the position-velocity trajectories and electronic wave functions. From the wave functions, we calculate the optical properties through Kubo-Greenwood relations. The principal Hugoniot, calculated from the FTDF-MD equation of state, agrees with gas-gun and recent laser-shock experiments for pressures up to 50 GPa. However, the maximum compression of the FTDF-MD Hugoniot (4.6 at 52 GPa) significantly differs from that of the laser shock experiment (6 at about 150 GPa). On the other hand, the optical reflectivities show reasonable agreement with the laser measurements for pressures up to 70 GPa. The system smoothly dissociates along the Hugoniot with the electrical conductivity reaching a value of $4000 \Omega^{-1} \text{cm}^{-1}$ at maximum compression. The fluid resembles that observed in the multiple-shock gas gun experiments comprising a soup of transiently interacting monomers and dimers. We also obtain good agreement with previous tight-binding and *ab initio* molecular dynamics studies.

ACKNOWLEDGMENTS

We thank Dr. P. Celliers and Dr. R. Cauble for kindly sending tabular data of NOVA experiments and Dr. P. Milonni for useful discussions on the optical properties. This work was performed under the auspices of the U.S. Department of Energy through Los Alamos and Lawrence Livermore National Laboratories (Contract No. W-7405-Eng-36).

*Present address: Corning Incorporated, Corning, NY 14831.

¹H. K. Mao and R. J. Hemley, *Rev. Mod. Phys.* **66**, 671 (1994).

²J. D. Lindl, R. L. McCoy, and E. M. Campbell, *Phys. Today* **45** (9), 32 (1992).

³W. J. Nellis, S. T. Weir, and A. C. Mitchell, *Science* **273**, 936 (1996).

⁴*Megagauss Technology and Pulse Power Applications*, edited by C. M. Fowler, R. S. Card, and D. J. Erickson (Plenum, New York, 1992).

⁵N. C. Holmes, M. Ross, and W. J. Nellis, *Phys. Rev. B* **52**, 15 835 (1995).

⁶S. T. Weir, A. C. Mitchell, and W. J. Nellis, *Phys. Rev. Lett.* **76**, 1860 (1996).

⁷V. Ya. Ternovoi, A. S. Filimonov, V. E. Fortov, S. V. Kvitov, D. N. Nikolaev, and A. A. Pyalling, *Physica B* **265**, 6 (1999).

⁸L. B. DaSilva, P. Celliers, G. W. Collins, K. S. Budil, N. C. Holmes, T. W. Barbee, Jr., B. A. Hammel, J. D. Kilkenny, R. J. Wallace, M. Ross, R. Cauble, A. Ng, and G. Chiu, *Phys. Rev. Lett.* **78**, 483 (1997); G. W. Collins, L. B. DaSilva, P. Celliers, D. M. Gold, M. E. Foord, R. J. Wallace, A. Ng, S. V. Weber, K. S. Budil, and R. Cauble, *Science* **281**, 1178 (1998).

⁹P. M. Celliers, G. W. Collins, L. B. DaSilva, D. M. Gold, R. Cauble, R. J. Wallace, M. E. Foord, and B. A. Hammel, *Phys. Rev. Lett.* **84**, 5564 (2000).

¹⁰SESAME: The Los Alamos Scientific Laboratory, Equation of State Database, Report No. LA-UR-92-3407 (unpublished); G. I. Kerley in *Molecular-Based Study of Fluids*, edited by J. M.

Haile and G. A. Mansoori (American Chemical Society, Washington, D.C., 1983), pp. 107–138.

¹¹W. R. Magro, D. M. Ceperley, C. Pierleoni, and B. Bernu, *Phys. Rev. Lett.* **76**, 1240 (1996); C. Pierleoni, D. M. Ceperley, B. Bernu, and W. R. Magro, *ibid.* **73**, 2145 (1994).

¹²B. Militzer and D. Ceperley, *Phys. Rev. Lett.* **85**, 1890 (2000); B. Militzer and E. Pollock, *Phys. Rev. E* **61**, 3470 (2000).

¹³L. Collins, I. Kwon, J. Kress, N. Troullier, and D. Lynch, *Phys. Rev. E* **52**, 6202 (1995); L. Collins, J. Kress, T. Lenosky, N. Troullier, and I. Kwon, *J. Comput.-Aided Mater. Des.* **5**, 173 (1998); L. Collins, J. Kress, S. Bickham, T. Lenosky, and N. Troullier, *High Press. Res.* **16**, 313 (2000).

¹⁴I. Kwon, L. Collins, J. Kress, and N. Troullier, *Phys. Rev. E* **54**, 2844 (1996).

¹⁵D. Hohl, V. Natoli, D. M. Ceperley, and R. M. Martin, *Phys. Rev. Lett.* **71**, 541 (1993).

¹⁶J. Kohanoff and J-P. Hansen, *Phys. Rev. E* **54**, 768 (1995).

¹⁷O. Pfaffenzeller and D. Hohl, *J. Phys.: Condens. Matter* **9**, 11 023 (1997).

¹⁸T. Lenosky, S. Bickham, J. Kress, and L. Collins, *Phys. Rev. B* **61**, 1 (2000).

¹⁹G. Galli, R. Hood, A. Hazi, and F. Gygi, *Phys. Rev. B* **61**, 909 (2000).

²⁰S. Bagnier, P. Blottiau, and J. Clerouin, *Phys. Rev. E* **63**, 015301 (2000).

²¹J. I. Penman, J. Clerouin, and G. Zerah, *Phys. Rev. E* **51**, R5224 (1994).

- ²²D. Klakow, C. Toepffer, and P.-G. Reinhard, Phys. Lett. A **192**, 55 (1994); J. Chem. Phys. **101**, 10 766 (1994).
- ²³I. Kwon, J. D. Kress, and L. A. Collins, Phys. Rev. B **50**, 9118 (1994).
- ²⁴T. J. Lenosky, J. D. Kress, L. A. Collins, and I. Kwon, J. Quant. Spectrosc. Radiat. Transf. **58**, 743 (1997); Phys. Rev. B **55**, 11 907 (1997); T. J. Lenosky, J. D. Kress, and L. A. Collins, *ibid.* **56**, 5164 (1997).
- ²⁵T. J. Lenosky, J. D. Kress, L. A. Collins, R. Redmer, and H. Juranek, Phys. Rev. E **60**, 1665 (1999).
- ²⁶A. Bunker, S. Nagel, R. Redmer, and G. Röpke, Phys. Rev. B **56**, 3094 (1997); A. Bunker, S. Nagel, R. Redmer, and G. Röpke, Contrib. Plasma Phys. **37**, 115 (1997); **37**, 469(E) (1997); S. Nagel, R. Redmer, G. Röpke, M. Knaup, and C. Toepffer, Phys. Rev. E **57**, 5572 (1998).
- ²⁷M. Ross, Phys. Rev. B **54**, R9589 (1996).
- ²⁸D. Saumon, W. B. Hubbard, G. Chabrier, and H. M. van Horn, Astrophys. J. **391**, 827 (1992).
- ²⁹I. Kwon, J. Kress, and L. Collins, Phys. Rev. B **52**, 15 165 (1995).
- ³⁰S. R. Bickham, O. Pfaffenzeller, L. A. Collins, J. D. Kress, and D. Hohl, Phys. Rev. B **58**, R11 813 (1998).
- ³¹J. Kress, S. Mazevet, L. Collins, and W. Wood, Phys. Rev. B **63**, 024302 (2001).
- ³²J. Kress, S. Bickham, L. Collins, B. Holian, and S. Goedecker, Phys. Rev. Lett. **83**, 3896 (1999); S. Bickham, J. Kress, and L. Collins, J. Chem. Phys. **112**, 9695 (2000).
- ³³S. Bickham, J. Kress, L. Collins, and R. Stumpf, Phys. Rev. Lett. **83**, 568 (1999).
- ³⁴M. P. Allen and D. J. Tildesley, *Computer Simulations of Liquids* (Clarendon Press, Oxford, 1987).
- ³⁵N. D. Mermin, Phys. Rev. **137**, A1441 (1965).
- ³⁶R. Wentzcovitch, J. L. Martins, and P. B. Allen, Phys. Rev. B **45**, 11 372 (1992); R. M. Wentzcovitch and J. L. Martins, Solid State Commun. **78**, 831 (1991).
- ³⁷J. P. Perdew, J. A. Chevary, S. H. Vosko, K. A. Jackson, M. R. Pedersen, D. J. Singh, and C. Fiolhais, Phys. Rev. B **46**, 6671 (1992).
- ³⁸N. Troullier and J. L. Martins, Phys. Rev. B **43**, 1993 (1991).
- ³⁹D. Vanderbilt, Phys. Rev. B **41**, 7892 (1990).
- ⁴⁰G. Kresse and J. Hafner, J. Phys.: Condens. Matter **6**, 8245 (1994).
- ⁴¹O. H. Nielsen and R. M. Martin, Phys. Rev. B **32**, 3780 (1985); **32**, 3792 (1985).
- ⁴²D. C. Rapaport, *The Art of Molecular Dynamics Simulations* (Cambridge University Press, Cambridge, 1995).
- ⁴³W. A. Harrison, *Solid State Theory* (McGraw-Hill, New York, 1970).
- ⁴⁴N. W. Ashcroft and N. D. Mermin, *Solid State Physics* (Saunders, Philadelphia, 1976).
- ⁴⁵J. Callaway, *Quantum Theory of the Solid State* (Academic Press, New York, 1974), Sec. 6.5.
- ⁴⁶G. Kresse and J. Hafner, Phys. Rev. B **47**, R558 (1993); G. Kresse and J. Furthmüller, Comput. Mater. Sci. **6**, 15 (1996); G. Kresse and J. Furthmüller, Phys. Rev. B **54**, 11 169 (1996).
- ⁴⁷N. Troullier, pw6: Finite-temperature density functional molecular dynamics program (1999).
- ⁴⁸T. N. Rescigno, Phys. Rev. Lett. **84**, 4377 (2000).
- ⁴⁹M. A. Berkovsky, Physica A **214**, 461 (1995).
- ⁵⁰Z. Lin and J. Harris, J. Phys.: Condens. Matter **4**, 1055 (1992).
- ⁵¹M. Ross, L. H. Yang, and G. Galli, J. Phys. IV **10**, Pr5-281 (2000).